Controlled Formation of Native Defects in Ultrapure ZnO for the Assignment of Green Emissions to Oxygen Vacancies

Fredeŕic Averseng, Miao Zhang, Frederic Averseng, Jean-Marc Krafft, Patrizia Borghetti, Guylène Costentin, Slavica Stankic

Controlled Formation of Native Defects in Ultrapure ZnO for the Assignment of Green Emissions to Oxygen Vacancies

Miao Zhang[1,2], Frédéric Averseng[1], Jean-Marc Krafft[1], Patrizia Borghetti[2], Guylène Costentin[1*] and Slavica Stankic[2*]

[1]Sorbonne Université, CNRS, Laboratoire de Réactivité de Surface, LRS, F-75005 Paris, France

[2]Sorbonne Université, CNRS, Institut des NanoSciences de Paris, INSP, F-75005 Paris, France.

[*]Corresponding authors: slavica.stankic@insp.jussieu.fr and guylene.costentin@upmc.fr

ABSTRACT

Ultrapure ZnO nanopowders were synthesized via vapor-phase based methods under oxygen deficient conditions. The type and relative proportions of intrinsic point defects were studied by photoluminescence (PL) and EPR spectroscopies performed under strictly controlled conditions. Besides coupled PL/EPR signals recently assigned to Zn_i^+ (2.80 eV / $\boldsymbol{g}$=1.96) two green emissions were systematically detected at 2.50 eV and 2.22 eV without EPR counterparts whereas their contributions were observed to depend on synthesis' oxygen partial pressure (P_{O2}). Among diamagnetic defects likely to be formed in O_2-poor conditions, Zn_i^0 and Zn_i^{2+} were discarded based on their reported energy levels – with transitions associated rather to match the violet light. Conversely, the involvement of oxygen vacancies (V_O^0 and V_O^{2+}) as recombination centers for the green emission in ZnO was supported by Raman and XPS data. In line with the expected trends based on formation energies, the always dominant green luminescence (2.50 eV) was assigned to V_O^{2+} and the weaker one (2.22 eV) to V_O^0. The involvement of an electron containing defect (V_O^0) was confirmed by visible light absorption observed in DR UV-Vis spectra. We also showed that the Zn_i^+/ V_O^{2+} ratio can be tuned by P_{O2} or by the choice of static or flow synthesis conditions. Overall, this study demonstrates that by controlling the conditions during synthesis, processing and spectroscopic investigations, the

ultrapure ZnO nanopowders represent reliable models for the identification of photoluminescent crystal defects – an approach that can be widely applied on other systems.

INTRODUCTION

Optical materials encompass a broad field of applications such as lasers, sensors, optical waveguides, imaging systems, optical fibers, and new, cutting-edge applications. In that respect, ZnO plays one of the leading roles since it exhibits unique optical properties that include high optical transmittance in visible and near IR-region, high electrical conductivity, large exciton binding energy at room temperature (60 meV), etc. Moreover, ZnO can emit light that covers almost the full visible part of the electromagnetic spectrum with photoluminescence (PL) emissions ranging from violet (430-440 nm), over green (495-515 nm) to yellow (600 nm) as recently reported for ZnO nanotetrapods.[1] Intensities and energies of these PL emissions are highly governed by the atomic-scale defects, which were shown to strongly depend on the material's preparation and processing conditions.

Among the PL bands generally detected in ZnO, the green luminescence (GL) is probably the most controversially discussed one. Many researchers ascribed impurities, such as copper, to green luminescence.[2-3] However, being also detected in non-doped ZnO crystals,[4-10] the additional involvement of intrinsic defects has also been proposed. Yet, even when considering the sole intrinsic defects, the controversy still exists. For instance, the green emissions at 520 nm (2.38 eV) and 540 nm (2.29 eV) – observed in non-doped ZnO powders, thin films and single crystals –were assigned to oxygen or zinc vacancies (V_O and V_{Zn}, respectively), oxygen anti-sites (O_{Zn}) or oxygen interstitial (O_i).[7, 9, 11-15]

By using ultrapure ZnO produced by combustion of metallic zinc in controlled atmosphere, the presence of elements other than Zn and O, *i.e.* extrinsic defects, is thus excluded. We have recently demonstrated[1] that a native defect is responsible for the GL at 495 nm (2.50 eV) in ZnO smoke whereas an additional thermal annealing led to GL at 515 nm (2.41 eV). The latter was attributed to Vo^+ but the origin of the GL at 2.50 eV, detected in the as-synthesized ZnO smoke, remained uncertain. The occurrence of such types of defects strongly dependents on Zn and/or O_2 concentration and the aim of the present study is to investigate the influence of synthesis conditions (O_2 partial pressure) on the type and concentration of defects in ZnO powders, in order to better assess the origin of GL luminescence. For that purpose, a comparative study has been conducted on ZnO samples free of extrinsic defects. They were prepared by combustion of metallic Zn in different O_2/Ar ratio either in a glove-box (via glove-box combustion, GBC) or in a flow-reactor (via chemical vapor synthesis, CVS). The syntheses were conducted under static (total pressure of 1 bar) or dynamic (under gas flow with reduced total pressure of 50 mbar) conditions to produce smoke and CVS samples, respectively. In addition, given that the CVS synthesis method was shown to produce smaller and more homogeneous MgO nanopowders than the GBC one,[16-17] the comparison of the corresponding ZnO powders provides the opportunity to investigate if the particle size may also affect the optical properties of ZnO. We also applied high-vacuum conditions ($P < 10^{-5}$ mbar) during the storage, handling and all spectroscopic characterizations. Such precaution plays a key role for the identification of defects[1] since an interaction of native defects with environmental molecules (O_2, H_2O, CO_2 etc.) could otherwise lead to the transformation either of defect's oxidation state ($Zn_i^0 \overset{O_2}{\rightarrow} Zn_i^+$)[18] or chemical identity ($V_O \overset{H_2O}{\longrightarrow} OH$).[19-20] Finally, in order to get deeper into the nature of defects responsible for GL in ZnO, PL data were combined with EPR ones obtained under the same conditions. This approach allowed us to unravel the origin of two green

emissions typically detected at 495 nm (2.50 eV) and 560 nm (2.22 eV) in ZnO nanopowders obtained by gas-phase based synthesis techniques.

2. EXPERIMENTAL SECTION

2.1 Synthesis and storage

Glove Box Combustion (GBC): smoke-5 and smoke-50 were fabricated by burning Zn-foil (high purity: 99.99%, 0.125 mm thickness, Advent Research Materials Ltd) in a glove box made of stainless steel and designed to afford primary vacuum ($P \sim 10^{-1}$ mbar). After three alternating cycles (outgassing and purging with Ar), an Ar/O_2 mixture (Air liquide, purity Ar > 99.99 % and O_2 > 99.995 %) was introduced into the glove box up to P = 1 bar. The combustion of Zn was then performed in two different Ar/O_2 ratios in order to obtain smoke-5 (Ar/O_2 = 95/5) and smoke-50 (Ar/O_2 = 50/50). More details about the powders synthesis are given in Reference [17]. As confirmed by XPS analysis, the applied synthesis conditions ensure that ZnO samples are free of extrinsic defects.[1]

Chemical Vapor Synthesis (CVS)*:* CVS-powders were fabricated in a flow reactor which allows Zn-combustion in different Ar/O_2 ratios. The two samples were synthesized under the same Ar-flow (1000 sccm) while the oxygen flow was doubled (from 500 to 1000 sccm) for CVS-1 and CVS-2, respectively. Details of the CVS synthesis method are provided in references [21-22]. Please note, that the CVS-reactor is pre-evacuated while the stream of Ar/O_2 is applied before the Zn-evaporation starts. Such a constant purging guaranties conditions in which ultra-pure powders can be obtained. The evaporation temperature of metallic Zn was chosen as to correspond to a Zn-vapor pressure of 1 mm Hg column (1.33 mbar). Given the low total pressure during CVS process (50 mbar) both CVS samples are synthesized in poorer O_2 conditions compared to those of smoke samples.

During the storage, handling and all spectroscopic measurements, the ZnO powders were constantly maintained under dynamic vacuum conditions ($P < 10^{-5}$ mbar). Such a caution, together with the synthesis methods ensure that all the spectroscopic features described below originate from ultrapure ZnO powders.

2.2 Characterizations

Transmission Electron Microscopy (TEM). For the purpose of microscopic studies, as-synthesized ZnO powders were directly deposited on TEM grids, preventing the use of any solvent. TEM measurements were performed on a JEOL 2100 field emission transmission electron microscope operating at 200 kV with a 0.18 nm resolution.

Electron Paramagnetic Resonance (EPR). For the purpose of subsequent electronic paramagnetic spectroscopy (EPR) studies, the ZnO samples were introduced in a suprasil quartz tube (5 mm external diameter) that was directly connected to a homemade high-vacuum ($P < 10^{-5}$ mbar) line in order to avoid any external contamination, providing thus uniform experimental conditions to compare the samples. The EPR measurements were performed on a JEOL FA300 computerized spectrometer working at ~9.3 GHz (X-band). The presented spectra were all recorded placing the powders under dynamic vacuum ($P < 10^{-5}$ mbar) at 77 K, using an insertion dewar containing liquid nitrogen, and by applying a microwave power of 2 mW and 100 kHz field modulation. In order to avoid the overmodulation and subsequent alteration of narrow EPR signals, a modulation width/amplitude of 0.1mT was systematically used. The g-factors were calibrated by using solid 2,2-diphenyl-1-picrylhydrazyl (DPPH) and care was taken to always keep the same height of powder in the EPR tube (~2 cm). Computer simulations of the spectra were performed using the EPRsim32 program.[23]

Diffuse Reflectance UV-vis (DR UV-Vis). The spectra were acquired at room temperature using a Varian Cary 5000 spectrometer equipped with an integrating sphere, while a sample of barium sulfate ($BaSO_4$) with ~100 % reflectance was used as a reference.

Photoluminescence (PL). Room-temperature experiments were performed on a Fluorolog II fluorometer (Jobin-Yvon) equipped with a 450 W Xe lamp as an excitation source. Most of the photoluminescence emission spectra were obtained setting the excitation energy at 4.13 eV (300 nm) and using a WG-320 cut-off filter on the emission side to prevent the contributions of the first- and second-order coming from the excitation light. When operating with an excitation energy of 3.10 eV (400 nm), a WG-410 cut-off filter was used. The PL band fitting analyses were done using IGOR.

Diffuse reflectance UV-vis and Photoluminescence measurements were carried out in a quartz glass tube that was connected to the same homemade high vacuum line ($P < 10^{-5}$ mbar) as that used for EPR measurements.

X-Ray Photoelectron Spectroscopy (XPS). XPS spectra were obtained with a non-monochromatic Al Kα source (photon energy, hν = 1486.7 eV) and a hemispherical analyzer Phoibos 100 with a pass energy of 20 eV at normal emission. The stoichiometric ratio n_{Zn}/n_O between two species distributed homogeneously in the sample is obtained through the following equation: $n_{Zn}/n_O = I_{Zn}(\sigma_O\lambda_O T_O)/I_O(\sigma_{Zn}\lambda_{Zn}T_{Zn})$, where I_{Zn} is the integration area of the peak Zn 2p and I_O that of the component of O 1s corresponding to lattice oxygen in ZnO, T is the transmission function of the analyzer tabulated for the analyzer Phoibos 100, λ_{Zn} and λ_O are provided by the NIST standard reference database for the ZnO material[24-25] while σ_{Zn} and σ_O are taken from reference.[26] XPS spectra were obtained in UHV conditions comprising $P < 10^{-9}$ mbar.

3. RESULTS AND DISCUSSION

3.1. Influence of the preparation conditions on morphological properties

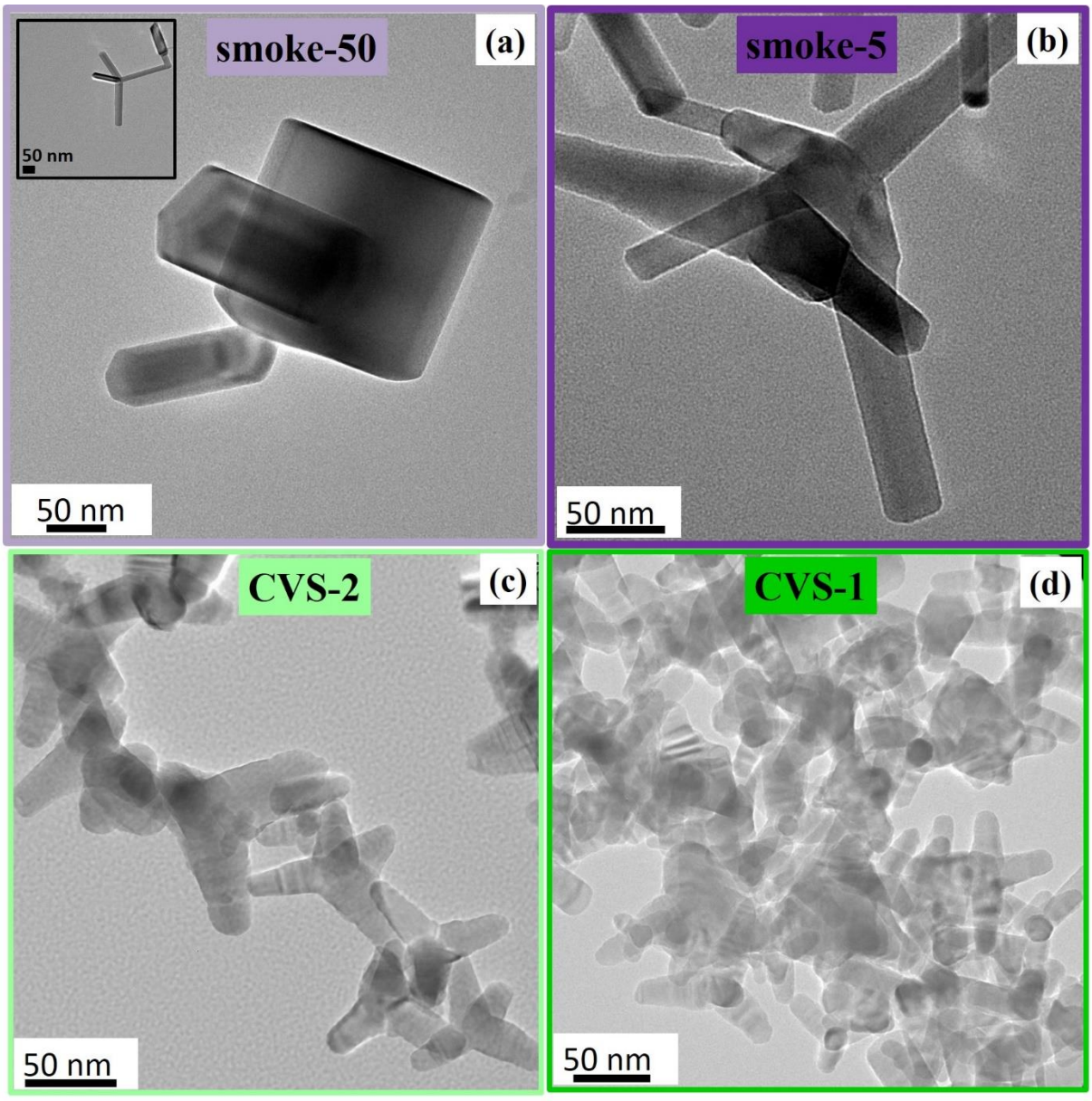

Figure 1: TEM images of ZnO nanopowders. (a) smoke-50, (b) smoke-5, (c) CVS-2 and (d) CVS-1.

Representative TEM images of the four studied samples are shown in Figure 1. Tetrapod-like shapes dominate in all nanopowders except in smoke-50 (Figure 1a). Typical of combustion synthesis, tetrapods exhibit four hexagonal arms that originate from the center of a polyhedron. The length of these arms differs from sample to sample and may exceed 100 nm while, in all samples, the corresponding diameter is lower than 50 nm. The size of the tetrapods in CVS

powders is observed to be smaller and more homogeneous than in smoke samples, with strongly stepped arms not exceeding 50 nm in length. Tetrapods can also be observed in TEM images of the sample that was obtained in the richest O_2-conditions *i.e.* smoke-50 (inset in Figure 1a). However, hexagonal prisms, some of which look like pseudo-cubes, dominate in this nanopowder (Figure 1a). The associated HRTEM and electron diffraction diagram (Figure S1) are consistent with the ZnO wurtzite structure. The same is concluded from their corresponding XRD diffractograms which all show only one set of peaks, all in line with the wurzite ZnO (not shown). Interestingly, the pseudo-cubic atypical particle's shape seen in TEM images of smoke-50 can be explained by reducing the contribution of the one of two non-polar facets in hexagonal ZnO – as obtained through Wulff shape constructions shown in Figure S2. In this figure, the (11-20) orientation is totally eliminated for the sake of clarity. To our knowledge, such shapes have not been observed up to now in samples obtained by vapor-phased techniques but rather reported for samples grown by hydrothermal routes.[27-29] Tetrapod morphology is typically reported for ZnO smoke fabricated by Zn-combustion in air (hereafter referred to as smoke-air). These tetrapodal particles exhibit multi-facet single crystals involving (10-10), (11-20), (0001) and (000-1) surfaces with the polar orientations corresponding only to 25% of the total surface area.[30] Given that half of the polar faces in ZnO equilibrium shape (hexagonal prisms, Figure S1a) are expected to be terminated by oxygen (000-1), the tendency for their junction resulting into tetrapods might be related to relaxation effect counterbalancing the lack of oxygen within the combustion synthesis. Such an oxygen limitation effect no longer occurs in the richer O_2 conditions applied for the synthesis of smoke-50 that most certainly explains the shape of this sample in form of separated hexagonal prisms. The difference in shape of ZnO particles highlights how the nucleation-growth process within combustion syntheses is affected by oxygen partial pressure. Apart from affecting the particle's shape, the surface topology is also

altered by the synthesis conditions – as illustrated by the formation of steps on the surfaces of the CVS samples (Figure 1c, 1d).

3.2 Identification of native defects

Apart from line defects, *i.e.* steps observed on the CVS samples, the occurrence of point defects is strongly suggested by the different colors of all samples. Indeed, except for the perfectly white smoke-50, yellow turns more and more vivid when going from smoke-5 (pale yellow), over CVS-2 (strong yellowish) to CVS-1 (almost orange), strongly reflecting their defective structure. Both synthesis techniques occur far from thermodynamic equilibrium and include rapid quenching conditions while Zn-rich (O_2-poor) conditions can be generally considered.[31-32] Hence, formation of defects such as zinc interstitials and/ or oxygen vacancies is expected in the course of both synthesis routes. Kohan et al. [33]calculated the concentration of defects as a function of P_{O2} and showed that the concentration of Zn_i and Vo is expected to increase as P_{O2} decreases during the synthesis. In contrast, the concentration of O_i and V_{Zn} – that preferentially occur in an O_2-rich atmosphere – was calculated to strongly drop off with decreasing P_{O2}.[33] These latter defects are therefore excluded as potential candidates in our samples.

DR UV-Vis spectroscopy. In agreement with the evolution of the sample's color, a red shifted absorption edge is observed for smoke-5 and the two CVS samples compared to smoke-50 (Figure 2). The corresponding band gap values (E_{bg}), determined from Tauc plots and provided in Figure S3, are lower than that reported for bulk ZnO (3.37 eV).[34] While the value obtained for smoke-50 (3.26 eV) is quite close to that reported for ZnO smoke-air (3.25 eV),[1] it shifts to 3.23 eV and 3.17 eV for smoke-5 and the two CVS samples, respectively. In agreement with previous studies,[35-37] all these features indicate that structural defects are present in all ZnO samples. In particular, the band gap narrowing and visible light absorption may be correlated with oxygen vacancies – as reported by both DFT[38] and experimental studies.[39]

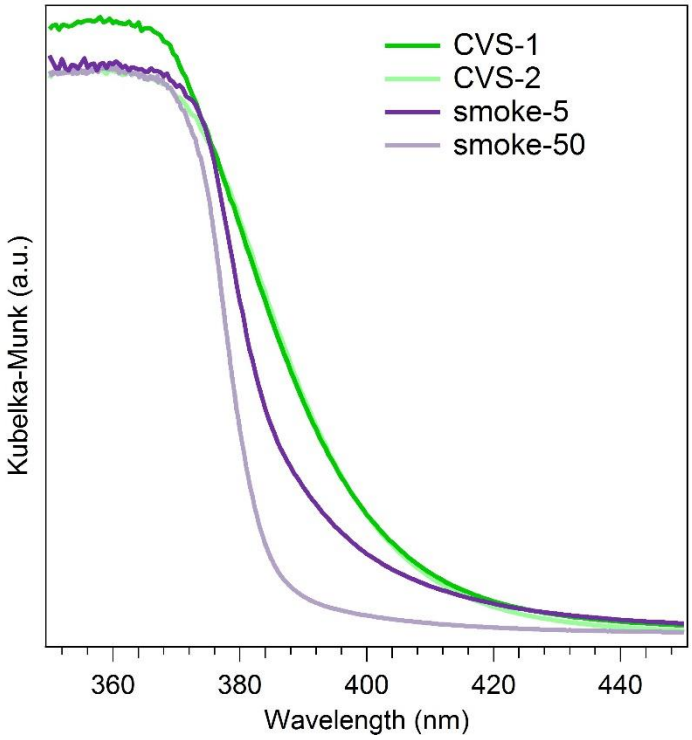

Figure 2: DR UV-Vis spectra of smoke-5, smoke-50, CVS-2 and CVS-1.

Deeper understanding of the nature of native defects in semiconducting materials can be beneficially achieved by combining two complementary techniques, namely PL and EPR spectroscopies.[1, 40]

EPR. One should first note that, among zinc interstitials and oxygen vacancies, only Zn_i^+ and V_O^+ are paramagnetic, hence EPR-active. Similar to smoke-air, EPR spectra of the four samples (Figure 3) reveal two signals, an intense one at g ~1.956 and a much weaker one at g ~ 1.960 that were both recently ascribed to Zn_i^+ defects.[1] The signals are observed at g = 1.958 and 1.964 in spectra of CVS samples which can be ascribed to slightly different local environment in samples of different morphology. Moreover, both signals are much more intense for CVS samples than for the smoke ones. Given that the formation of Zn_i^+ defects is favored in oxygen poor conditions, this once more underlines that the conditions provided within CVS synthesis are, by far, less rich in oxygen than those of GBC. Except in the case of smoke-air that reveals lower EPR signal compared to all samples, the trend in the intensity of EPR signal as a function

of oxygen partial pressure is as expected: CVS-1 ~ CVS-2 >> smoke-5 > smoke-50. Finally, an absence of EPR signal at g = 2.002 confirms what ~~it~~ was observed for smoke-air [1]: V_O^+ species is absent in the as-prepared ZnO samples.

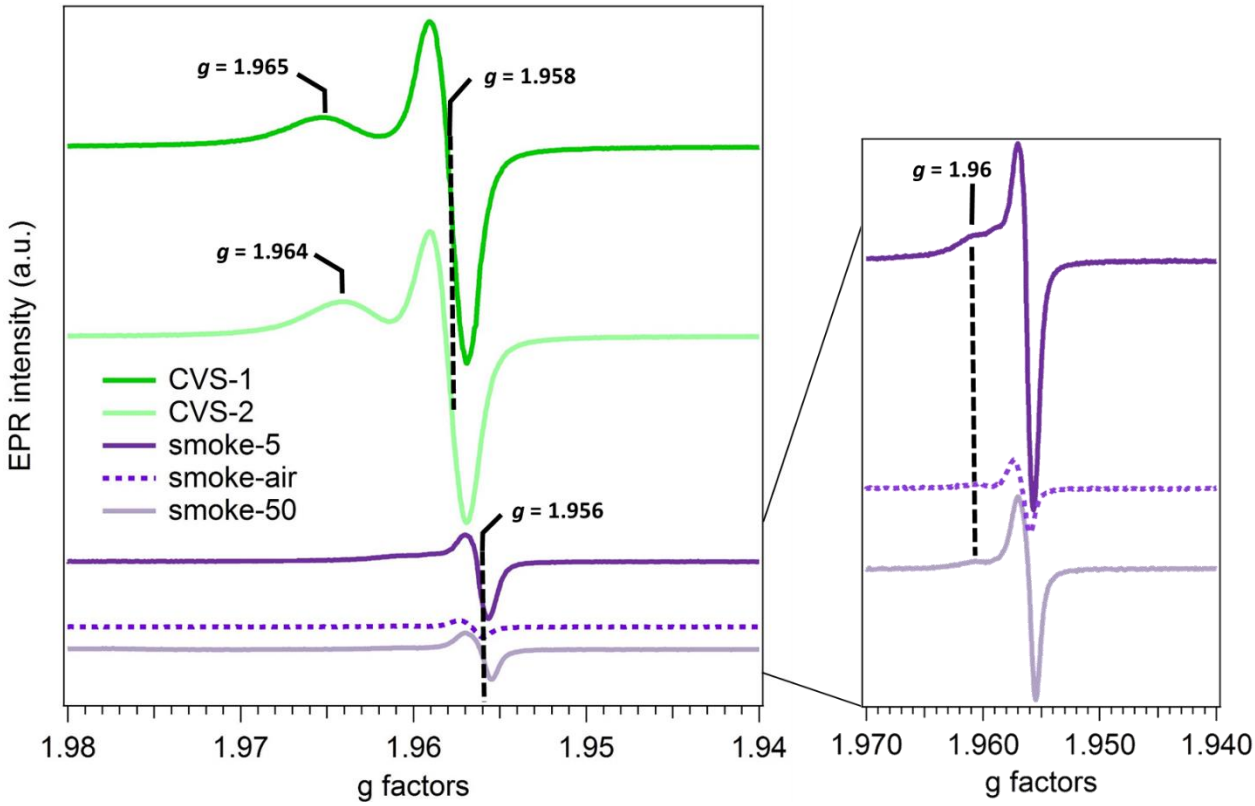

Figure 3: 77K EPR spectra of smoke-5, smoke-50, CVS-2 and CVS-1 compared to that of smoke-air. The right part of the figure corresponds to zoomed EPR spectra of smoke-5 and smoke-50.

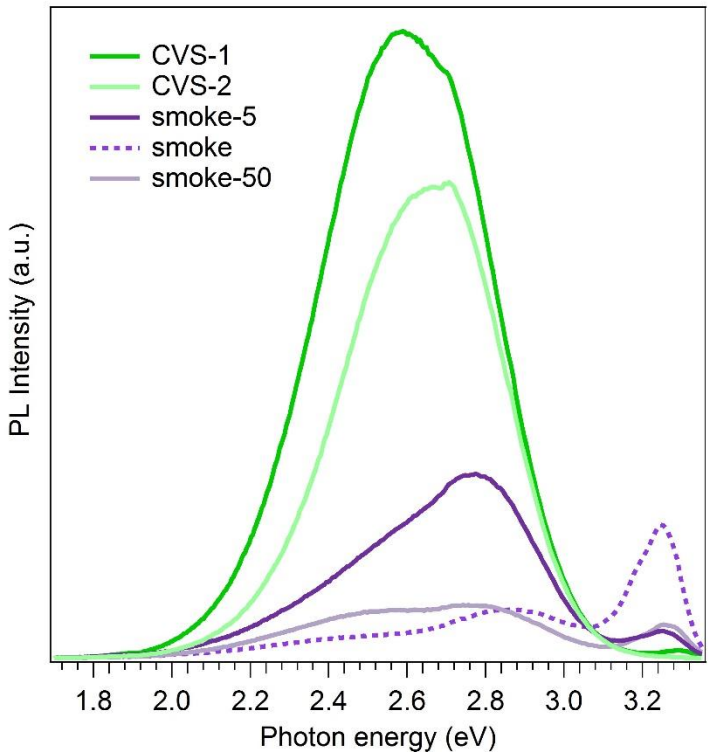

Figure 4: RT-PL spectra of smoke-5, smoke-50, CVS-1 and CVS-2 compared to that of smoke-air. PL spectra are obtained at E_{EXC} = 4.13 eV.

PL. PL spectra of the four ZnO samples recorded at E_{EXC} = 4.13 eV ($E_{EXC} > E_{BG}$) are shown in Figure 4 and compared to the spectrum of ZnO smoke-air (dashed violet curve) that was previously reported in Ref.[1] PL spectra of all samples consist of two parts: UV and visible PL emissions. The fundamental ZnO emission at ~ 3.3 eV (UV band) corresponds to a direct recombination between the conduction band (CB) and the valence band (VB) and its intensity represents a direct measure of the crystal quality. On the contrary, the presence of visible bands in PL spectra indicates that recombination pathways involve additional discrete energy levels within the band gap of the semiconducting material. Defects in material's crystal structure create such additional energy states. In contrast to smoke-air, the UV emission band of the four other samples is much weaker compared to the visible PL band. In CVS samples, the UV-

emission band is even almost undetectable. Interestingly, based on relative intensity of the UV towards visible PL emission, smoke-50 appears more defective than smoke-air. Such a tendency, fully consistent with that observed by EPR (Figure 3), may appear quite surprising at first glance, since smoke-50 is prepared in an oxygen partial pressure that is higher than that used for smoke-air. However, the presence of water traces in air may passivate the native defects, so that ZnO produced by Zn-combustion in air (smoke-air) appears less defective. Indeed, oxygen vacancies were shown to be easily filled in upon water dissociation.[1, 19, 41]

The loss of the UV contribution clearly benefits to the visible emission, with increasing intensity in the order: smoke-50 < smoke-5 < CVS-2 < CVS-1. The shape of the visible PL emission is also greatly modified along the same series. In CVS samples, the visible emission presents a broad, multicomponent band with a maximum between ~2.5-2.7 eV. Similarly, the visible PL emission of smoke-5 is also asymmetric yet the main contribution is rather centered at ~2.8 eV (violet luminescence, VL). On the contrary, in PL spectrum of smoke-50 the visible PL band is better resolved and, clearly, exhibits two maxima, at 2.50 eV (GL) and 2.8 eV (VL). Such a tendency shows that the PL signals are less sensitive to particle's size and distribution than to P_{O2}. The detection of PL band at 2.8 eV in all samples is consistent with that of EPR signal at g~ 1.96. An identical PL/EPR couple has been recently detected in smoke-air and assigned to Zn_i^+ defects.[1] PL properties of smoke-50 and smoke-5 were further examined by using E_{EXC} = 3.10 eV (λ_{EXC} = 400 nm), *i.e.* an energy that is lower than their corresponding band gap energies determined from Tauc (Figure S3). The two samples were selected for the PL excitation under visible light, since the difference in absorption edge and the corresponding shift towards visible light was observed to be the strongest between two GBC samples (Figure 2). In Figure 5, PL spectra recorded at E_{EXC} = 3.10 eV on smoke-50 and smoke-5 are compared to those obtained with E_{EXC} = 4.13 eV and previously shown in Figure 4.

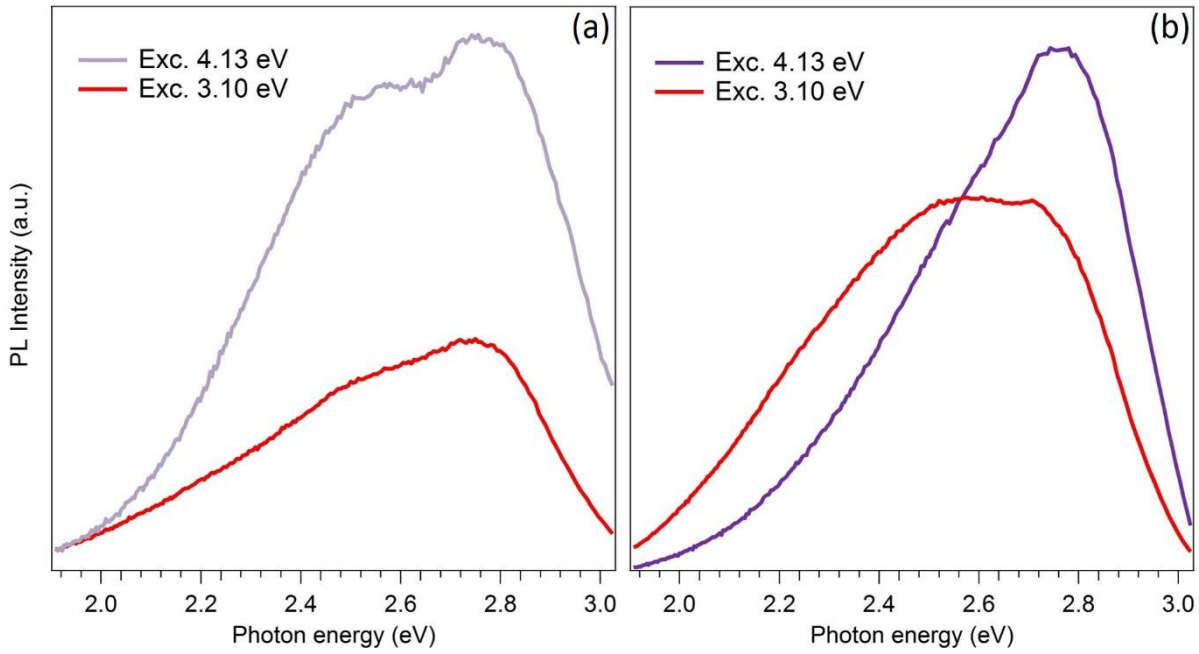

Figure 5: RT-PL spectra obtained at E_{EXC} = 4.13 eV and E_{EXC} = 3.10 eV for a) smoke-50 and b) smoke-5.

In the case of smoke-50, the decrease of the excitation energy down to 3.10 eV ($E_{EXC} < E_{BG}$) results in a less intense PL spectrum yet of similar shape to that obtained with E_{EXC}= 4.13 eV (Figure 5a). On the contrary, the PL properties of smoke-5 are much more affected by the reduction of E_{EXC}. Figure 5b shows that the excitation of this sample with an energy lower than E_{BG} reduces the relative contribution of VL at the benefit of the GL emission, especially in its lower-energy part, around 2.2 eV.

The corresponding band fitting analysis results in three Gaussian bands (Figure 6). The contributions peaking at 2.50 (GL) and 2.80 eV (VL) were previously reported also for smoke-air[1] while the second GL contribution at 2.22 eV was not mentioned. Besides, such Gaussian component at 2.22 eV is even also required to perfectly reproduce the low energy part of its PL spectrum recorded at 4.13 eV i.e. when using $E_{EXC} > E_{BG}$ (Figure 7b). Comparison of Figures

6 and 7b illustrates how using an excitation energy lower than E_{BG} favors the two GL emissions (2.22 and 2.50 eV).

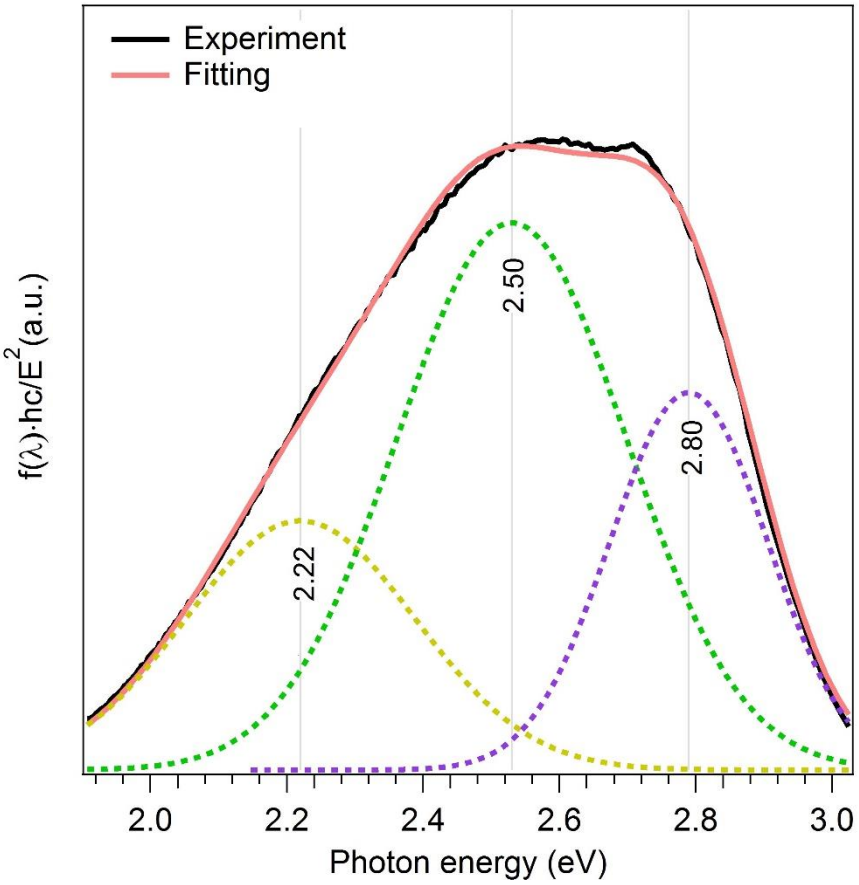

Figure 6: Band fitting analysis of PL spectrum of smoke-5 recorded at E_{EXC} = 3.10 eV (400 nm). Dashed curves correspond to the fitted contributions for individual emission components.

Interestingly, the involvment of the 2.22 eV contribution improves the band fitting analysis for all smoke and CVS samples (Figure 7) which points out the presence of defects associated with this energy in all the studied powders. The integration areas of the three Gaussian components extracted from the fittings of original spectra (Figure 7) are gathered in Table 1. Total contribution of these components increases with the decrease of P_{O2} used during the synthesis. The same trend is obtained for each individual Gaussian component, except for the 2.8 eV contribution (associated with Zn_i^+) of the two CVS samples. The tendency of PL at 2.8 eV in CVS samples is consistent with the same trend found in the intensity of the corresponding EPR

signal at g ~1.96 (Figure 3). The proportion of the 2.8 eV component globally decreases from the smoke to the CVS samples at the benefit of the two GL contributions at 2.50 and 2.22 eV. Note however that the proportion of signal at 2.8 eV significantly increases from smoke-50 to smoke-5 while it decreases from CVS-2 to CVS-1. Considering the two GL emissions, the one at 2.50 eV is always stronger than that at 2.22 eV. The latter is always the minor component and its relative proportion of ~13% in smoke-50 decreases down to 4-5 % in CVS samples.

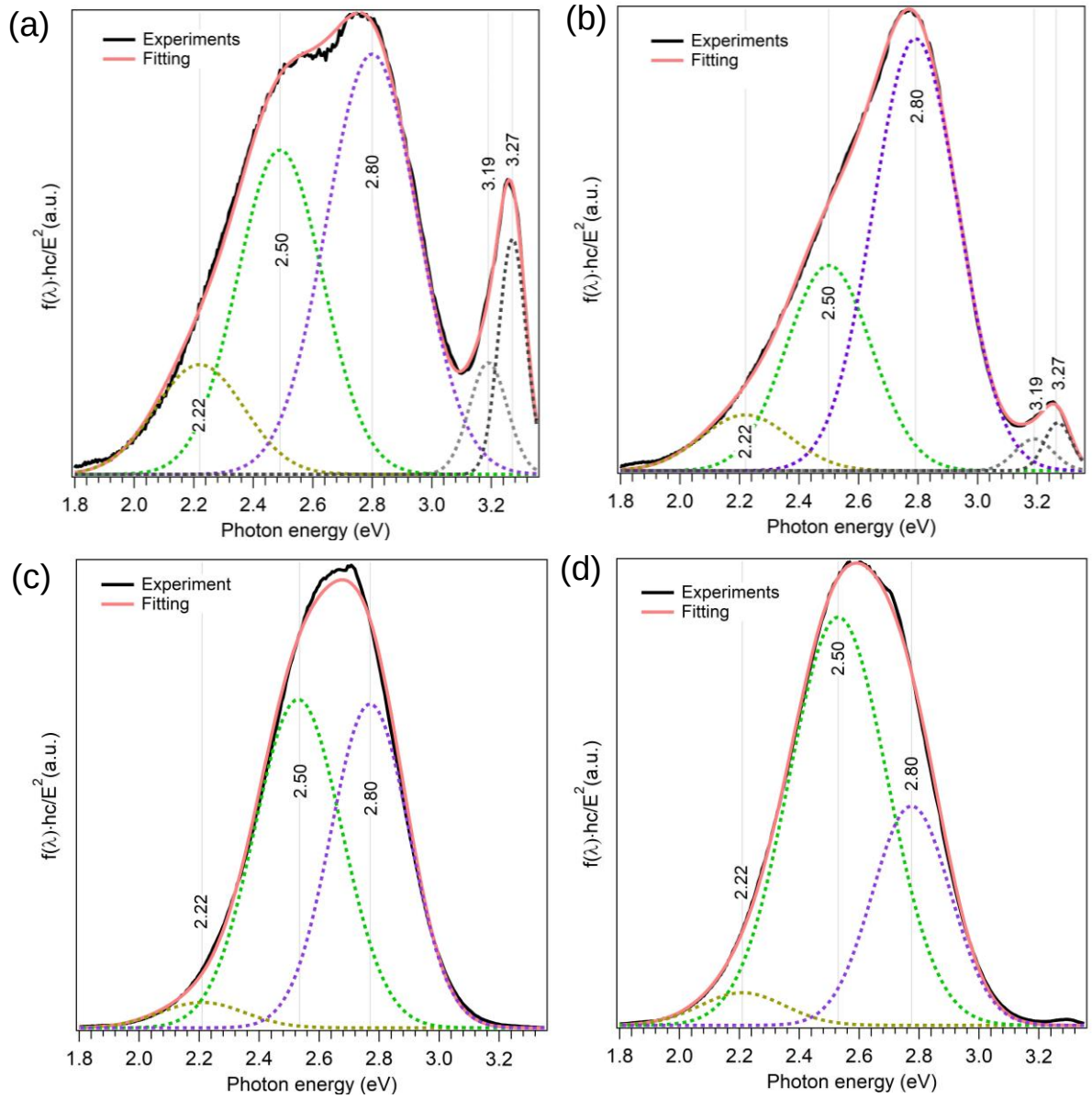

Figure 7: Band fitting analysis of PL spectra recorded at E_{EXC} = 4.13 eV of (a) smoke-50, (b) smoke-5, (c) CVS-2 and (d) CVS-1. For a sake of clarity, the spectra have been normalized on

their maximum of intensity. Dashed curves correspond to the fitted contributions for individual emission components.

Table 1: Integration area and relative proportions deduced from the original PL spectra fitting (E_{Exc} = 4.13 eV) of the smoke and CVS samples.

				PO_2 increase	
ZnO sample		smoke-50	smoke-5	CVS-2	CVS-1
Area of PL contribution	2.8 eV	0.83	2.77	4.90	4.32
	2.50 eV	0.60	1.31	5.51	10.10
	2.22 eV	0.21	0.37	0.42	0.70
Total area		1.64	4.45	10.83	15.12
Relative proportions	2.8/2.5/2.22	50/37/13	62/30/8	45/51/4	28/67/5

GL assignment. The detection of VL band at 2.8 eV in all samples is consistent with that of EPR signals at g ~ 1.96. An identical PL/EPR couple has been recently detected in smoke-air and assigned to Zn_i^+ defects.[1] Though previously observed for ZnO smoke-air, the origin of GL emission at 2.50 eV remained uncertain up to now. Therefore, this GL emission and the newly revealed one peaking at 2.22 eV deserve further discussion.

Hydrogen related defects have been proposed by the surface science community to be present in ZnO.[42-46] Even if we cannot not totally exclude any hydrogen trace, in the lack of any specific EPR hyperfine doublet,[47] the enhanced contribution of GL emissions at 2.50 and 2.22 eV in samples fabricated at significantly lower P_{O2} (i.e. in CVS samples) rather supports their assignment to defects that typically form in such conditions, namely zinc interstitial or oxygen vacancy. In contrast to VL (2.8 eV), these GL bands were observed without an EPR counterpart. Hence, Zn_i^0 or Zn_i^{2+} zinc interstitials as well as V_O^{2+} or V_O^0 oxygen vacancies appear as potential candidates for these green emissions since being all EPR silent. As it was experimentally demonstrated by Zeng and co.[31] and, also, calculated by several groups,[48-50] the

Zn_i-related energy levels fall around the conduction band minimum irrespectively of their oxidation state.[51-52] Consequently, Zn_i-related transitions rather match with violet-blue emission spectral range (405-465 nm i.e. 3.06-2.66 eV) so that these defects can be discarded as responsible for GL emissions. Therefore, the only remaining candidates at the origin of the PL bands at 2.50 eV and 2.22 eV are V_O^{2+} and V_O^0 oxygen vacancies. The favored presence of these type of defects in low P_{O2} synthesis conditions is further supported by Raman spectroscopy, as illustrated in Figure S4 that compares Raman spectra of smoke-50 and smoke-5. Indeed, the only difference between the two spectra concerns the band representative of oxygen motion in ZnO lattice (E_2^{high} mode). Its lower contribution in smoke-5 spectrum indicates a lack of lattice oxygen in this sample. This tendency is also confirmed by XPS analysis (Figure S5), with a higher Zn/O ratio in smoke-5 (1.16) than in smoke-50 (1.01).

The assignment of each of the two GL emission can also be discussed considering the formation energies of V_O^{2+} and V_O^0 defects in ZnO. The lowest formation energy in Zn-rich conditions among the three types of oxygen vacancies was calculated for Vo^{2+}. [48, 53-54] Thus, it is expected to prevail over the neutral one (V_O^0) in our ZnO samples. On this basis, the GL at 2.50 eV, that is detected with higher intensity compared to the GL at 2.22 eV in all smoke and CVS samples, including smoke-air,[1] can be associated with V_O^{2+}. The origin of the second GL at 2.22 eV can therefore be ascribed to Vo^0, usually considered as a deep donor.[55] Moreover, both DFT and experimental studies[38, 55-56] ascribed the extension of absorptions towards visible light (Figure 2) to oxygen vacancies, in particular to V_O^0. Indeed, electron containing states within the band gap (which is typically the case for V_O^0) are required in this absorption process and lead to sample's coloration. Such a contribution of neutral oxygen vacancies (V_O^0) in ZnO samples prepared in low P_{O2} is in line with the modification of optical properties observed on ZnO single crystals after annealing treatment in Zn vapor.[15]

As summarized in Table 2 and illustrated in simplified energy levels diagram (Figure S6), the green luminescence of smoke and CVS ZnO involves three contributions associated to the three types of oxygen vacancies. The 2.22 and 2.50 eV GL contributions are observed in as-synthesized ZnO powders therefore implying that V_O^0 and V_O^{2+} exist as native defects. On the contrary, the GL with the maximum at 2.41 eV – that was observed in smoke-air only after sample's annealing in vacuum or Zn vapor and ascribed to single charged oxygen vacancy V_O^+ – was once again never observed in as-synthesized samples, in line with the absence of the corresponding EPR signal at g = 2.002. This is in agreement with its high formation energy, and the tendency to decay into Vo^0 or Vo^{2+} due to its thermodynamic instability.[1, 53] Recently, an evolution of 2.4 eV PL was also observed in Ar irradiated ZnO and in line with results obtained by positron annihilation spectroscopy also assigned to oxygen vacancies.[47]

Table 2: Assignment of the GL emissions in ZnO nanoparticles prepared by combustion of metallic zinc

GL emission	2.22 eV	2.50 eV	2.41 eV
ZnO Oxygen vacancy	V_O^0	V_O^{2+}	V_O^+
Observed in samples	As-prepared		Vacuum/Zn annealing

4. CONCLUSION

PL/EPR features were investigated in ZnO ultrapure nanopowders prepared by the combustion of metallic Zn in various oxygen partial pressures. Yellowish ZnO nanopowders with tetrapod-like shapes were generally obtained. Yet, the synthesis performed under the highest PO_2 resulted in white powder rich in hexagonal prisms. Irrespectively of the synthesis

conditions, PL/EPR features were observed to be qualitatively the same in all the studied samples which points out on the same type of defects. The total concentration of defects – being reflected through the total PL and EPR contributions – was shown to be dramatically enhanced as the P_{O2} used during the synthesis drops.

Previously ascribed to Zn_i^+ defects, the PL/EPR couple with ~ 2.8 eV / g ~ 1.96 was observed to dominate in ZnO powders produced under static conditions while GL emission with no EPR counterparts prevailed in CVS powders. Beside the violet, the visible PL emission was shown to consist of two additional green components (2.50 and 2.22 eV) while the VL/GL relative ratio could be tuned. Among the defects likely to be formed in the synthesis conditions applied here (Zn-rich/O_2-poor), Zn interstitials as potential candidates for GL were discarded. This is in line with their energy levels which rather result in violet emission. Consequently and supported by Raman spectroscopy, GL at 2.50 eV and 2.22 eV were respectively assigned to V_O^{2+} and V_O^0. The discrimination between the two oxygen vacancies and the corresponding assignment were based on their different relative contributions in conjunction with different formation energies ($V_O^{2+} < V_O^0$). Indeed, in all analyzed spectra, the GL at 2.50 eV dominates over that at 2.22 eV. Assigned to V_O^0, i.e to an electron-containing defect, the PL at 2.22 eV also provides an explanation for the optical absorption in the visible part of the spectrum.

Overall, this study sheds light on the V_O-related origin of green emissions in ZnO and shows that, under strictly controlled experimental conditions, ZnO ultrapure nanopowders can be successfully used as model systems for studying optically active crystal defects.

ACKNOWLEDGMENT

Dr. Miao Zhang wants to thank the China Scholarship Council (CSC) for the three years Ph.D. founding. The authors are also grateful to: Dominique Demaille from Institut des NanoSciences de Paris, Sorbonne Université, (INSP) for the TEM data collection and interpretation, Vincent

Losinho from Laboratoire de Réactivité de Surface, Sorbonne Université, (LRS) for his help in designing and building the set up used for EPR and PL *in situ* studies and Stephane Chenot from Institut des NanoSciences de Paris, Sorbonne Université, (INSP) for the maintenance of synthesis chambers and high-vacuum storage lines.

REFERENCES

1. Zhang, M.; Averseng, F.; Haque, F.; Borghetti, P.; Krafft, J. M.; Baptiste, B.; Costentin, G.; Stankic, S., Defect-Related Multicolour Emissions in ZnO Smoke: From Violet, over Green to Yellow. *Nanoscale* **2019**, *11*, 5102-5115.
2. Garces, N. Y.; Wang, L.; Bai, L.; Giles, N. C.; Halliburton, L. E.; Cantwell, G., Role of Copper in the Green Luminescence from ZnO Crystals *Appl. Phys. Lett.* **2002**, *81*, 622-624.
3. Muthukumaran, S.; Gopalakrishnan, R., Structural, FTIR and Photoluminescence Studies of Cu Doped ZnO Nanopowders by Co-Precipitation Method. *Opt. Mater.* **2012**, *34*, 1946-1953.
4. Guo, H. L.; Zhu, Q.; Wu, X. L.; Jiang, Y. F.; Xie, X.; Xu, A. W., Oxygen Deficient ZnO $_{1-X}$ Nanosheets with High Visible Light Photocatalytic Activity. *Nanoscale* **2015**, *7*, 7216-7223.
5. Camarda, P.; Messina, F.; Vaccaro, L.; Agnello, S.; Buscarino, G.; Schneider, R.; Popescu, R.; Gerthsen, D.; Lorenzi, R.; Gelardi, F. M., Luminescence Mechanisms of Defective ZnO Nanoparticles. *Phys. Chem. Chem. Phys.* **2016**, *18*, 16237-16244.
6. Gurwitz, R.; Cohen, R.; Shalish, I., Interaction of Light with the ZnO Surface: Photon Induced Oxygen "Breathing," Oxygen Vacancies, Persistent Photoconductivity, and Persistent Photovoltage. *J. Appl. Phys.* **2014**, *115*, 033701/1-033701/9.
7. Borseth, T. M.; Svensson, B. G.; Kuznetsov, A. Y.; Klason, P.; Zhao, Q. X.; Willander, M., Identification of Oxygen and Zinc Vacancy Optical Signals in ZnO. *Appl. Phys. Lett.* **2006**, *89*, 262112-1-262112-3.
8. Tam, K. H., et al., Defects in ZnO Nanorods Prepared by a Hydrothermal Metho. *J. Phys. Chem. B* **2006**, *110*, 20865-20871.
9. Lin, B.; Fu, Z.; Jia, Y., Green Luminescent Center in Undoped Zinc Oxide Films Deposited on Silicon Substrates. *Appl. Phys. Lett.* **2001**, *79*, 943-945.
10. Lv, J.; Li, C., Evidences of Vo, Vzn, and Oi Defects as the Green Luminescence Origins in ZnO *Appl. Phys. Lett.* **2013**, *103*, 232114/1-232114/5.
11. Tay, Y. Y.; Tan, T. T.; Boey, F.; Liang, M. H.; Ye, J.; Zhao, Y.; Norby, T.; Li, S., Correlation between the Characteristic Green Emissions and Specific Defects of ZnO. *Phys. Chem.Chem. Phys.* **2010**, *12*, 2373-2379.
12. Wang, D.; Seo, H. W.; Tin, C. C.; Bozack, M. J.; Williams, J. R.; Park, M.; Sathitsuksanoh, N.; Cheng, A. J.; Tzeng, Y. H., Effects of Postgrowth Annealing Treatment on the Photoluminescence of Zinc Oxide Nanorods. *J. Appl. Phys.* **2006**, *99*, 113509/1-113509/5.
13. Ton-That, C.; Weston, L.; Phillips, M. R., Characteristics of Point Defects in the Green Luminescence from Zn-and O-Rich ZnO. *Phys. Rev. B* **2012**, *86*, 115205/1-115205/5.
14. Jayakumar, O. D.; Sudarsan, V.; Sudakar, C.; Naik, R.; Vatsa, R. K.; Tyagi, A. K., Green Emission from ZnO Nanorods: Role of Defects and Morphology. *Scripta Mater.* **2010**, *62*, 662-665.
15. Čížek, J.; Valenta, J.; Hruška, P.; Melikhova, O.; Procházka, I.; Novotný, M.; Bulíř, J., Origin of Green Luminescence in Hydrothermally Grown ZnO Single Crystals. *Appl. Phys. Lett.* **2015**, *106*, 251902/1-251902/4.
16. Stankic, S.; Müller, M.; Diwald, O.; Sterrer, M.; Knözinger, E.; Bernardi, J., Size-Dependent Optical Properties of MgO nanocubes. *Angew.Chem.Int.Ed* **2005**, *44*, 4917 –4920.

17. Stankic, S.; Cottura, M.; Demaille, D.; Noguera, C.; Jupille, J., Nucleation and Growth Concepts Applied to the Formation of a Stoichiometric Compound in a Gas Phase: The Case of MgO Smoke. *J. Crystal Growth* **2011**, *329*, 52-56.
18. Tonezzer, M.; Lacerda, R. G., Integrated Zinc Oxide Nanowires/Carbon Microfiber Gas Sensors. *Sensors and Actuators, B: Chemical* **2010**, *150*, 517-522.
19. Kunat, M.; Girol, S. G.; Burghaus, U.; Woell, C., The Interaction of Water with the Oxygen-Terminated, Polar Surface of ZnO. *J. Phys. Chem. B* **2003**, *107*, 14350-14356.
20. Hu, H.; Ji, H. F.; Sun, Y., The Effect of Oxygen Vacancies on Water Wettability of a ZnO Surface. *Phys. Chem. Chem. Phys.* **2013**, *15*, 16557-16565.
21. Knoezinger, E.; Jacob, K. H.; Singh, S.; Hofmann, P., Hydroxyl Groups as Ir Active Surface Probes on MgO Crystallites. *Surf. Sci.* **1993**, *290*, 388-402.
22. Stankic, S.; Sternig, A.; Finocchi, F.; Bernardi, J.; Diwald, O., Zinc Oxide Scaffolds on MgO Nanocubes. *Nanotechnology* **2010**, *21*, 355603/1-355603/8.
23. Spałek, T.; Pietrzyk, P.; Sojka, Z., Application of the Genetic Algorithm Joint with the Powell Method to Nonlinear Least-Squares Fitting of Powder Epr Spectra. *J. Chem. Inf. Model* **2005**, *45*, 18-29.
24. Powell, C. J.; Jablonski, A., *Nist Electron Effective-Attenuation-Length Database - Version 1.3, National Institute of Standards and Technology.*: Gaithersburg, MD 2011.
25. Llovet, X.; Salvat, F.; Bote, D.; Salvat-Pujol, F.; Jablonski, A.; Powell, C. J., *Nist Database of Cross Sections for Inner-Shell Ionization by Electron or Positron Impact, Version 1.0, National Institute of Standards and Technology*: Gaithersburg, Maryland, 2014.
26. Yeh, J. J., *Atomic Calculation of Photoionization Cross-Sections and Asymmetry Parameters*, 1985.
27. Zhu, B. L.; Zhao, X. Z.; Su, F. H.; Li, G. H.; Wu, X. G.; Wu, J.; Wu, R., Low Temperature Annealing Effects on the Structure and Optical Properties of ZnO Films Grown by Pulsed Laser Deposition. *Vacuum* **2010**, *84*, 1280-1286.
28. Li, F.; Ding, Y.; Gao, P.; Xin, X.; Wang, Z. L., Single-Crystal Hexagonal Disks and Rings of ZnO: Low-Temperature, Large-Scale Synthesis and Growth Mechanism. *Angewandte Chemie, Intern. Ed.* **2004**, *43*, 5238-5242.
29. Li, Q.; Kumar, V.; Li, Y.; Zhang, H.; Marks, T. J.; Chang, R. P. H., Fabrication of ZnO Nanorods and Nanotubes in Aqueous Solutions *Chem. Mater.* **2005**, *17*, 1001-1006.
30. Haque, F.; Chenot, S.; Viñes, F.; Illas, F.; Stankic, S.; Jupille, J., ZnO Powders as Multi-Facet Single Crystals. *Phys. Chem. Chem. Phys.* **2017**, *19*, 10622-10628.
31. Zeng, H.; Duan, G.; Li, Y.; Yang, S.; Xu, X.; Cai, W., Blue Luminescence of ZnO Nanoparticles Based on Non‐Equilibrium Processes: Defect Origins and Emission Controls. *Adv.Func. Mater.* **2010**, *20*, 561-572.
32. Zeng, H.; Cai, W.; Liu, P.; Xu, X.; Zhou, H.; Klingshirn, C.; Kalt, H., ZnO-Based Hollow Nanoparticles by Selective Etching: Elimination and Reconstruction of Metal− Semiconductor Interface, Improvement of Blue Emission and Photocatalysis. *ACS nano* **2008**, *2*, 1661-1670.
33. Kohan, A. F.; Ceder, G.; Morgan, D.; Van de Walle, C. G., First-Principles Study of Native Point Defects in ZnO. *Phys. Rev. B* **2000**, *61*, 15019-15027.
34. Look, D. C.; Reynolds, D. C.; Sizelove, J. R.; Jones, R. L.; Litton, C. W.; Cantwell, G.; Harsch, W. C., Electrical Properties of Bulk ZnO *Solid State Comm.* **1998**, *105*, 399-401.
35. Roth, A. P.; Webb, J. B.; Williams, D. F., Band-Gap Narrowing in Heavily Defect-Doped ZnO. *Phys. Rev. B* **1982**, *25*, 7836-7839.
36. De Angelis, F.; Armelao, L., Optical Properties of ZnO Nanostructures: A Hybrid DFT/TDDFT Investigation. *Phys. Chem. Chem. Phys.* **2011**, *13*, 467-475.
37. Ansari, S. A.; Khan, M. M.; Kalathil, S.; Nisar, A.; Lee, J.; Cho, M. H., Oxygen Vacancy Induced Band Gap Narrowing of ZnO Nanostructures by an Electrochemically Active Biofilm *Nanoscale* **2013**, *5*, 9238-9246.
38. Sheetz, R. M.; Ponomareva, I.; Richter, E.; Andriotis, A.; Menon, M., Defect-Induced Optical Absorption in Visisble Range in ZnO Naowires. *Phys. Rev. B* **2009**, *80*, 195314-1-195414-4.

39. Wang, J.; Wang, Z.; Huang, B.; Ma, Y.; Liu, Y.; Qin, X.; Zhang, X.; Dai, Y., Oxygen Vacancy Induced Band-Gap Narrowing and Enhanced Visible Light Photocatalytic Activity of ZnO. *ACS Appl.Mater.& Interf.* **2012**, *4*, 4024-4030.
40. Drouilly, C.; Krafft, J. M.; Averseng, F.; Casale, S.; Bazer-Bachi, D.; Chizallet, C.; Lecocq, V.; Vezin, H.; Lauron-Pernot, H.; Costentin, G., ZnO Oxygen Vacancies Formation and Filling Followed by in Situ Photoluminescence and in Situ EPR. *J. Phys. Chem. C* **2012**, *116*, 21297-21307.
41. Drouilly, C.; Krafft, J. M.; Averseng, F.; Lauron-Pernot, H.; Bazer-Bachi, D.; Chizallet, C.; Lecocq, V.; Costentin, G., Role of Oxygen Vacancies in the Basicity of ZnO: From the Model Methylbutynol Conversion to the Ethanol Transformation Application. *Appl. Catal. A* **2013**, *453*, 121-129.
42. Li, Y. J.; Kaspar, T. C.; Droubay, T. C.; Joly, A. G.; Nachimuthu, P.; Zhu, Z.; Shutthanandan, V.; Chambers, S. A., A Study of H and D Doped ZnO Epitaxial Films Grown by Pulsed Laser Deposition. *J. Appl. Phys.* **2008**, *104*, 053711.
43. Li, Y. J.; Kaspar, T. C.; Droubay, T. C.; Zhu, Z.; Shutthanandan, V.; Nachimuthu, P.; Chambers, S. A., Electronic Properties of H and D Doped ZnO Epitaxial Films. *Appl. Phys. Lett.* **2008**, *92*, 152105.
44. Jokela, S. J.; McCluskey, M. D., Structure and Stability of O−H Donors in ZnO from High-Pressure and Infrared Spectroscopy. *Phys. Rev. B* **2005**, *72*, 113201.
45. Wôll, C., The Chemistry and Physics of Zinc Oxide Surfaces. *Progr. Surf. Sci.* **2007**, *82*, 55-120.
46. Noei, H.; Qiu, H.; Wang, Y.; Löffler, E.; Wöll, C.; Muhler, M., The Identification of Hydroxyl Groups on ZnO Nanoparticles by Infrared Spectroscopy. *Phys. Chem. Chem. Phys.* **2008**, *10*, 7092-7097.
47. Son, N. T.; Isoya, J.; Ivanov, I. G.; Ohshima, T.; Janzén, E., Hydrogen at Zinc Vacancy of ZnO: An EPR and Eseem Study. *AIP Conference Proceedings* **2014**, *1583*, 341-344.
48. Erhart, P.; Albe, K.; Klein, A., First-Principles Study of Intrinsic Point Defects in ZnO: Role of Band Structure, Volume Relaxation, and Finite-Size Effects. *Phys. Rev. B* **2006**, *73*, 205203/1-205203/9.
49. Zhang, S.; Wei, S.-H.; Zunger, A., Intrinsic n-Type Versus p-Type Doping Asymmetry and the Defect Physics of ZnO. *Phys. Rev. B* **2001**, *63*, 075205/1-075205/7.
50. Look, D. C.; Farlow, G. C.; Reunchan, P.; Limpijumnong, S.; Zhang, S. B.; Nordlund, K., Evidence for Native-Defect Donors in n-Type ZnO. *Phys. Rev. Lett.* **2005**, *95*, 225502/1-225502/4.
51. Epie, E.; Chu, W., Ionoluminescence Study of Zn− and O− Implanted ZnO Crystals: An Additional Perspective. *Appl. Surf. Sci.* **2016**, *371*, 28-34.
52. Gallino, F.; Pacchioni, G.; Di Valentin, C., Transition Levels of Defect Centers in ZnO by Hybrid Functionals and Localized Basis Set Approach. *J. Chem. Phys.* **2010**, *133*, 144512/1-144512/10.
53. Janotti, A.; Van de Walle, C. G., Native Point Defects in ZnO. *Phys. Rev. B* **2007**, *76*, 165202/1-165202/22. .
54. Vidya, R.; Ravindran, P.; Fjellvåg, H.; Svensson, B.; Monakhov, E.; Ganchenkova, M.; Nieminen, R. M., Energetics of Intrinsic Defects and Their Complexes in ZnO Investigated by Density Functional Calculations. *Phys. Rev. B* **2011**, *83*, 045206/1-045206/12.
55. Halliburton, L. E.; Giles, N. C.; Garces, N. Y.; Luo, M.; Xu, C.; Bai, L.; Boatner, L. A., Production of Native Donors in ZnO by Annealing at High Temperature in Zn Vapor. *Appl. Phys. Lett.* **2005**, *87*, 172108-1-172108-3.
56. Evans, S. M.; Giles, N. C.; Halliburton, L. E.; Kappers, L. A., Further Characterization of Oxygen Vacancies and Zinc Vacancies in Electron-Irradiated ZnO. *J. Appl. Phys.* **2008**, *103*, 043710/1-043710/7.

Supporting Information for

Controlled Formation of Native Defects in Ultrapure ZnO for the Assignment of Green Emissions to Oxygen Vacancies

Miao Zhang[1,2] Frédéric Averseng[1], Jean-Marc Krafft[1], Patrizia Borghetti[2], Guylène Costentin[1*] and Slavica Stankic[2*]

[1]Sorbonne Université, CNRS, Laboratoire de Réactivité de Surface, LRS, F-75005 Paris, France
[2]Sorbonne Université, CNRS, Institut des NanoSciences de Paris, INSP, F-75005 Paris, France.
[*]Corresponding authors: slavica.stankic@insp.jussieu.fr and guylene.costentin@upmc.fr

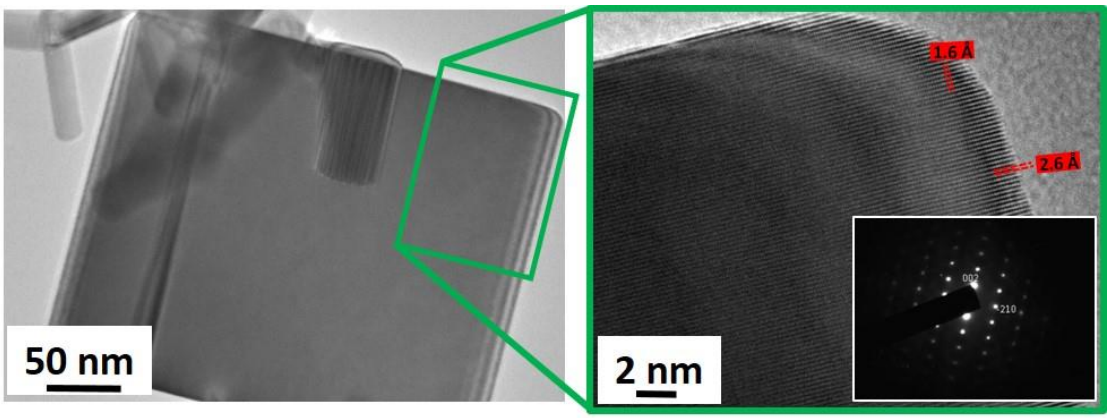

Figure S1. Representative TEM (a) and HRTEM (b) images of the as-synthesized smoke-50. HRTEM image (b) corresponds to the pseudo-cube viewed along a [120] zone axis of ZnO wurtzite structure. The inset in (c) shows SAED of the selected HRTEM zone in green.

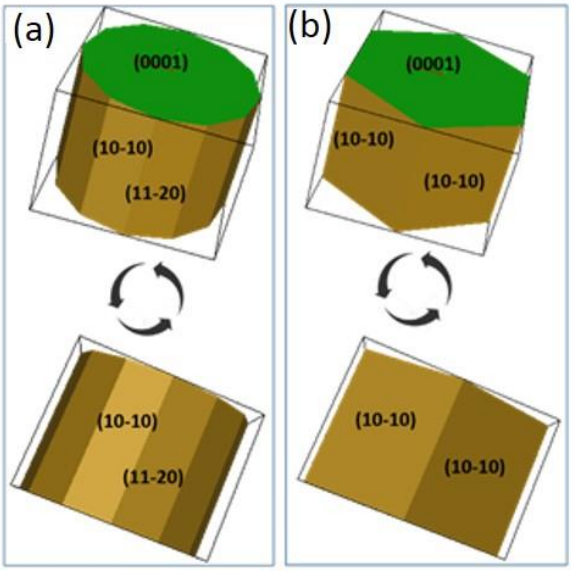

Figure S2. Wulff shape constructions for ZnO with different contributions of the non-polar faces: (a) the contribution of the two non-polar faces is equal, (b) the contribution of the (11-20) orientation is negligible. The shapes were rotated in order to illustrate how the hexagonal shape illustrated in (b) can appear as pseudocubic, such as those observed in TEM images of smoke-50 sample.

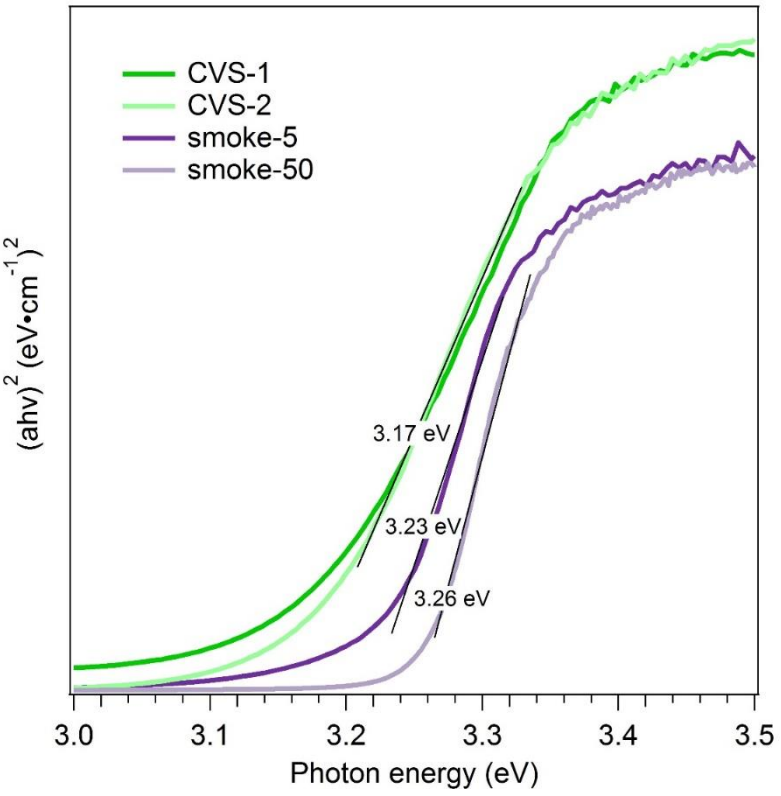

Figure S3. Tauc-plots of as-synthesized ZnO samples.

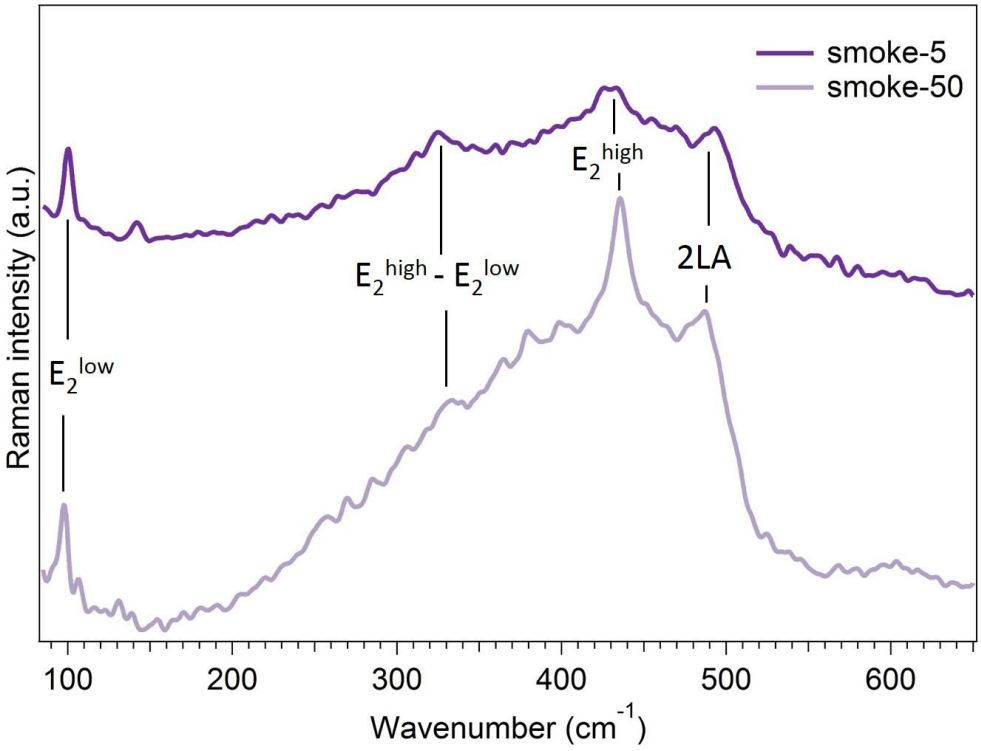

Figure S4. Raman spectra of as-synthesized smoke-50 and smoke-5.

In Raman spectrum of ZnO, the E_2^{low} and E_2^{high} mode are particularly sensitive to the motion of the lattice Zn and oxygen, respectively. According to Figure S3, in which Raman spectra of smoke-5 and smoke -50 are compared, a similar intensity is observed for the band at 100 cm^{-1} (E_2^{low} mode) in both spectra. However, the intensity of the band at 439 cm^{-1} (E_2^{high} mode) is significantly decreased in spectrum obtained on smoke-5 that is significant of the peculiar lack of lattice oxygen in this sample.

Raman spectra (Figure S4) were recorded at room temperature on a Jobin-Yvon triple-stage T64000 Raman spectrometer that is equipped with a CCD camera. An Argon laser monochromatic source (λ= 514.5 nm) was used. The same quartz glass cell as described for PL and UV experiments was also used for Raman investigations.

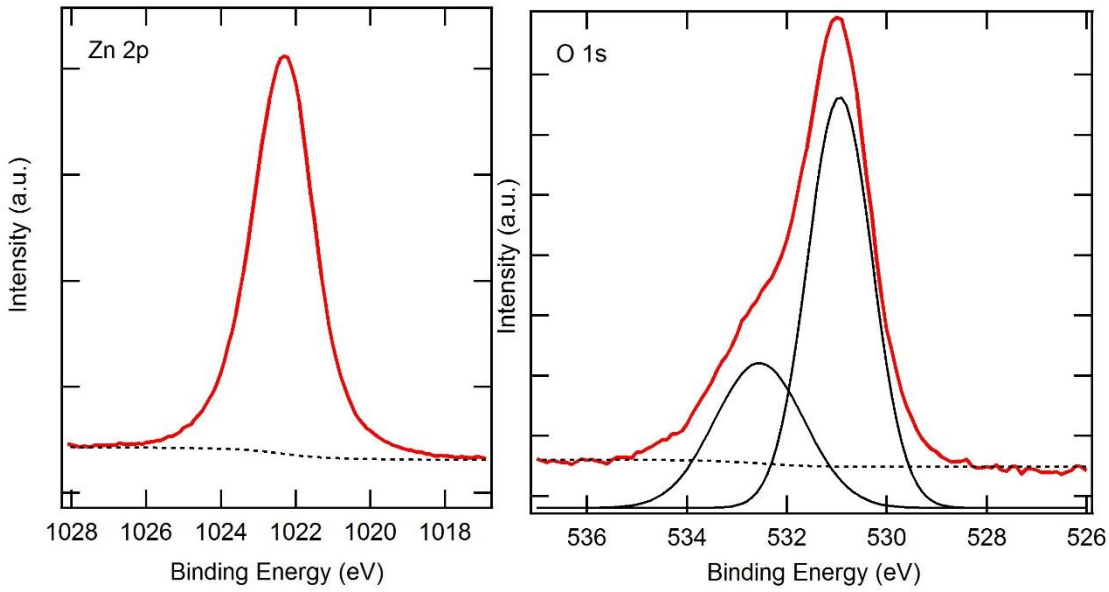

Figure S5**.** Zn 2p and O 1s XPS spectra of smoke-50 that were used to determine the surface stoichiometry. Red lines correspond to raw experimental data, dotted black lines is integral background, solid black lines are Gaussian curves used for fitting the experimental O 1s spectrum. The same procedure was applied for smoke-5.

The stoichiometric ratio was obtained through the following equation: $n_{Zn}/n_O = I_{Zn}(\sigma_O\lambda_O T_O)/I_O(\sigma_{Zn}\lambda_{Zn}T_{Zn})$ n1 / n2 = I1·(σ2·λ2·T2) / I2·(σ1·λ1·T1), where T is the transmission function of the analyzer tabulated for the analyzer Phoibos 100, λ_{Zn} and λ_O are provided by the NIST standard reference database for the ZnO material [1-2] while σ_{Zn} and σ_O are taken from reference.[3] Note that I_O is the integration areas of O 1s component which corresponds to lattice oxygen in ZnO (max. at 530.9 eV). This is obtained by fitting the O 1s spectrum with Gaussian curves. The second component of the O 1s (max. at 532.5 eV) was neglected since it corresponds to contamination occurred during the sample's exposure to the air while transferring into UHV chamber.

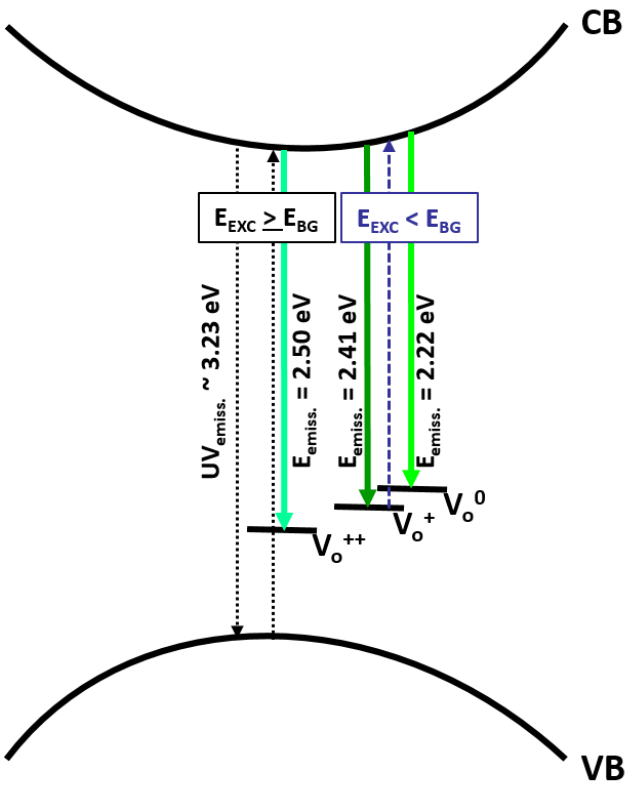

Figure S6: Simplified energy level diagram for oxygen vacancies observed in native ZnO samples prepared by Zn combustion methods.

Left-hand side of the diagram shows the transitions of electrons from valence to conduction band (black dotted arrow) that can be achieved only with excitation energy that is equal or larger than the band gap energy observed on here studied ZnO powders (3.17 – 3.26 eV). Right-hand side shows the transitions from electron containing defects (V_o^+ and V_o) into conduction band which, however, can be achieved with excitation energies that are lower than the E_{BG} (dark-blue dotted arrow). The excited electrons (from conduction band) recombine then with the defects that results in PL emission energies (green-colored solid arrows) different than the principal UV-emission in ZnO powders. This emission (~ 3.23 eV) can take place only under the $E_{EXC} > E_{BG}$ (illustrated with doted arrow at the left-hand side).

1. Powell, C. J.; Jablonski, A., *Nist Electron Effective-Attenuation-Length Database - Version 1.3, National Institute of Standards and Technology.*: Gaithersburg, MD 2011.
2. Llovet, X.; Salvat, F.; Bote, D.; Salvat-Pujol, F.; Jablonski, A.; Powell, C. J., *Nist Database of Cross Sections for Inner-Shell Ionization by Electron or Positron Impact, Version 1.0, National Institute of Standards and Technology*: Gaithersburg, Maryland, 2014.
3. Yeh, J. J., *Atomic Calculation of Photoionization Cross-Sections and Asymmetry Parameters*, 1985.